A Complete Model for Solid Cylindrical Magnetic Actuators*

Lei Zhu
Calnetix
12880 Moore Street
Cerritos, CA 90703, USA
lzhu@calnetix.com

Carl Knospe and Eric Maslen
Dept. of Mechanical and Aerospace Engineering
University of Virginia
Charlottesville, VA 22903, USA
Crk4y@virginia.edu & ehm7s@virginia.edu

***Abstract* – This paper presents a complete model for solid cylindrical magnetic actuators. The half-order model shows the eddy current effects on both the current stiffness and the displacement stiffness. Experiments conducted demonstrate the accuracy of the model.**

***Index Terms* – Eddy currents, displacement stiffness and current stiffness**

I. INTRODUCTION

In practice and in the literature, a magnetic levitation system operated in current mode is usually modelled by the block diagram shown in Fig. 1,

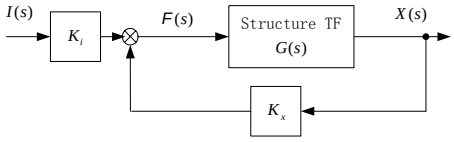

Fig. 1: Block Diagram for a Magnetic Actuator Operated in Current Model

In Fig. 1, the static gains K_i and K_x are generally called current stiffness and displacement stiffness in literature respectively, and are define as

$$K_i = \left.\frac{\partial f}{\partial i}\right|_{\substack{x=x_0\\ i=i_0}} \text{ and } K_x = \left.\frac{\partial f}{\partial x}\right|_{\substack{x=x_0\\ i=i_0}} \qquad (1)$$

This model is accurate only for laminated magnetic actuators where eddy currents may be ignored. The analytic results obtained in [1, 2] clearly demonstrate the effect of eddy currents on current-force relationship, when a solid actuator is employed.

In this paper, relation between displacement and mechanical force for solid cylindrical actuators of the geometry shown in Fig. 2, which is also the one used in [1], will be studied with eddy currents being taken into consideration.

II. EFFECT OF CHANGING AIR GAP ON MECHANICAL FORCE

* This work was supported by the National Science Foundation under Grant DMI-9988877.

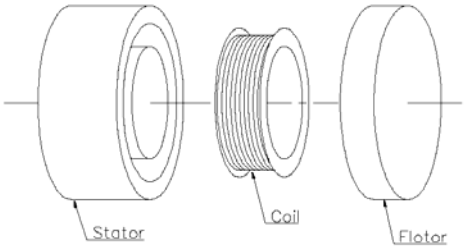

Fig. 2: Exploded View of A Solid Cylindrical Actuator

Suppose that the bias current I_b and the nominal air gap length g_n have been chosen for the solid cylindrical actuator. When there is a perturbation g_p to the nominal air gap, the flux inside the actuator will consist of two parts, the bias flux and the perturbation flux. The bias flux distribution will be the same as that examined in [1] when the frequency was zero, and the perturbation flux will be similar to that considered in [1] for the varying field. By superposition, the magnetic circuit approach employed in [1] may be used to develop a model for the relation between displacement and mechanical force, as will be demonstrated herein. In this paper, the actuator geometry division presented in [1] will be adopted and the effective reluctance of each element of the geometry developed in [1] will be used.

Select a small annular section of inner air gap at *r*. At any time *t*, the magnetomotive forces on the surfaces of the flotor and the stator consist of bias and perturbation terms:

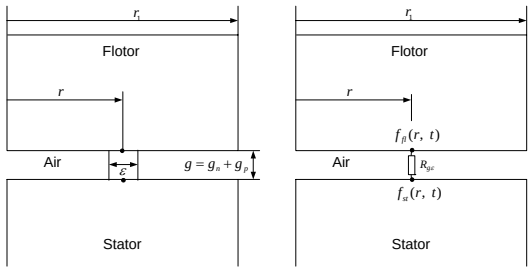

Fig. 3: Magnetomotive Force across a Small Annular Section of Inner Air Gap

$$f_{fl}(r,\ t) = f_{fl}^{b}(r) + f_{fl}^{p}(r,\ t) \qquad (2a)$$

$$f_{st}(r,\ t) = f_{st}^{b}(r) + f_{st}^{p}(r,\ t) \tag{2b}$$

Due to the perturbation of air gap length, the reluctance of the small annular air gap section may be written as

$$R_{g\varepsilon} = \frac{g_n + g_p(t)}{2\pi r \varepsilon \mu_0} \tag{3a}$$

Define the nominal reluctance of the gap section as

$$R_{g\varepsilon}^{n} = \frac{g_n}{2\pi r \varepsilon \mu_0} \tag{3b}$$

Assuming $g_p(t)$ is small, the flux passing through $R_{g\varepsilon}$ at any time *t*, is

$$\phi_\varepsilon(r,\ t) = \frac{f_{st}(r,\ t) - f_{fl}(r,\ t)}{R_{g\varepsilon}} \approx \frac{f_{st}(r,\ t) - f_{fl}(r,\ t)}{R_{g\varepsilon}^{n}} \cdot \left(1 - \frac{g_p(t)}{g_n}\right) \tag{4a}$$

Substituting (2) into (4a) yields

$$\begin{aligned} \phi_\varepsilon(r,\ t) = {} & \frac{1}{R_{g\varepsilon}^{n}} \cdot \left[f_{st}^{b}(r) - f_{fl}^{b}(r)\right] - \frac{1}{R_{g\varepsilon}^{n}} \cdot \left[f_{st}^{b}(r) - f_{fl}^{b}(r)\right] \cdot \frac{g_p(t)}{g_n} \\ & + \frac{1}{R_{g\varepsilon}^{n}} \cdot \left[f_{st}^{p}(r,\ t) - f_{fl}^{p}(r,\ t)\right] - \frac{1}{R_{g\varepsilon}^{n}} \cdot \left[f_{st}^{p}(r,\ t) - f_{fl}^{p}(r,\ t)\right] \cdot \frac{g_p(t)}{g_n} \end{aligned} \tag{4b}$$

Assuming the perturbation terms are small and then neglecting the higher order term, one may separate the flux into a time-invariant (bias) and time-varying (perturbation) components:

$$\phi_\varepsilon(r,\ t) = \phi_\varepsilon^{b}(r) + \phi_\varepsilon^{p}(r,\ t) \tag{5a}$$

$$\phi_\varepsilon^{b}(r) = \frac{1}{R_{g\varepsilon}^{n}} \cdot \left[f_{st}^{b}(r) - f_{fl}^{b}(r)\right] \tag{5b}$$

$$\begin{aligned} \phi_\varepsilon^{p}(r,\ t) = {} & -\frac{1}{R_{g\varepsilon}^{n}} \cdot \left[f_{st}^{b}(r) - f_{fl}^{b}(r)\right] \cdot \frac{g_p(t)}{g_n} \\ & + \frac{1}{R_{g\varepsilon}^{n}} \cdot \left[f_{st}^{p}(r,\ t) - f_{fl}^{p}(r,\ t)\right] \end{aligned} \tag{5c}$$

Assuming a uniform bias flux distribution in the air gaps yields

$$f_{st}^{b}(r) - f_{fl}^{b}(r) = \frac{NI_b R_1^0}{R^0} \tag{6}$$

where R^0 and R_1^0 are the static reluctances of the actuator flux path and Element 1 with fixed air gap g_n respectively. Combining (5) and (6) produces

$$\phi_\varepsilon^{b} = \frac{1}{R_{g\varepsilon}^{n}} \cdot \frac{NI_b R_1^0}{R^0} \tag{7a}$$

$$\phi_\varepsilon^{p}(r,\ t) = -\frac{1}{R_{g\varepsilon}^{n}} \cdot \frac{NI_b R_1^0}{R^0} \cdot \frac{g_p(t)}{g_n} + \frac{1}{R_{g\varepsilon}^{n}} \cdot \left[f_{st}^{p}(r,\ t) - f_{fl}^{p}(r,\ t)\right] \tag{7b}$$

Laplace transformation of (7b) yields

$$\begin{aligned} \phi_\varepsilon^{p}(r,\ s) &= L\left(\phi_\varepsilon^{p}(r,\ t)\right) \\ &= -\frac{1}{R_{g\varepsilon}^{n}} \cdot \frac{NI_b R_1^0}{R^0} \cdot \frac{g_p(s)}{g_n} + \frac{1}{R_{g\varepsilon}^{n}} \cdot \left[F_{st}^{p}(r,\ s) - F_{fl}^{p}(r,\ s)\right] \end{aligned} \tag{7c}$$

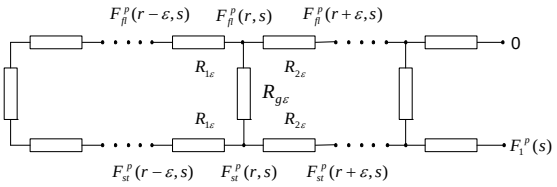

Fig. 4: Reluctance Network for Element 1

Using the reluctance network model of Element 1 shown in Fig. 4 and conservation of flux, one can obtain

$$\begin{aligned} & \phi_\varepsilon^{p}(r,\ s) + \frac{F_{st}^{p}(r,\ s) - F_{st}^{p}(r-\varepsilon,\ s)}{R_{1\varepsilon}} \\ & = \frac{F_{st}^{p}(r+\varepsilon,\ s) - F_{st}^{p}(r,\ s)}{R_{2\varepsilon}} \end{aligned} \tag{8}$$

Due to the symmetry of the reluctance network

$$F_{fl}^{p}(r,\ s) = F_1^{p}(s) - F_{st}^{p}(r,\ s) \tag{9}$$

Substituting (7c) and (9) into (8) yields

$$\begin{aligned} & \frac{F_{st}^{p}(r+\varepsilon,\ s) - F_{st}^{p}(r,\ s)}{R_{2\varepsilon}} = \frac{F_{st}^{p}(r,\ s) - F_{st}^{p}(r-\varepsilon,\ s)}{R_{1\varepsilon}} \\ & + \frac{2F_{st}^{p}(r,\ s)}{R_{g\varepsilon}^{n}} - \frac{F_1^{p}(s)}{R_{g\varepsilon}^{n}} - \frac{1}{R_{g\varepsilon}^{n}} \frac{NI_b R_1^0}{R^0} \cdot \frac{g_p(s)}{g_n} \end{aligned} \tag{10}$$

Taking the limit of (10) as $\varepsilon \to 0$ yields an ordinary differential equation

$$\begin{aligned} & \frac{d^2 F_{st}^{p}(r,\ s)}{dr^2} + \frac{1}{r}\frac{dF_{st}^{p}(r,\ s)}{dr} - \alpha_1^2 F_{st}^{p}(r,\ s) \\ & = -\frac{\alpha_1^2}{2} F_1^{p}(s) - \frac{\alpha_1^2}{2} \frac{NI_b R_1^0}{R^0} \cdot \frac{g_p(s)}{g_n} \end{aligned} \tag{11}$$

where $\alpha_1^2 = \dfrac{2\alpha}{\mu_r g_n}$. From the analysis in [1], the solution to (11) is clearly

$$F_{st}^{p}(r,\ s)=\frac{F_1^{p}(s)}{2}+\frac{1}{2}\frac{NI_bR_1^0}{R^0}\cdot\frac{g_p(s)}{g_n}+\left(\frac{F_1^{p}(s)}{2}-\frac{1}{2}\frac{NI_bR_1^0}{R^0}\cdot\frac{g_p(s)}{g_n}\right)\cdot\frac{I_0(\alpha_1 r)}{I_0(\alpha_1 r_1)} \quad (12a)$$

From (9) and (12a), we have

$$F_{fl}^{p}(r,\ s)=\frac{F_1^{p}(s)}{2}-\frac{1}{2}\frac{NI_bR_1^0}{R^0}\cdot\frac{g_p(s)}{g_n}-\left(\frac{F_1^{p}(s)}{2}-\frac{1}{2}\frac{NI_bR_1^0}{R^0}\cdot\frac{g_p(s)}{g_n}\right)\cdot\frac{I_0(\alpha_1 r)}{I_0(\alpha_1 r_1)} \quad (12b)$$

Substituting (12) into (7c) generates

$$\phi_{\varepsilon}^{p}(r,\ s)=\frac{1}{R_g^n}\cdot\left(F_1^{p}(s)-\frac{NI_bR_1^0}{R^0}\cdot\frac{g_p(s)}{g_n}\right)\cdot\frac{I_0(\alpha_1 r)}{I_0(\alpha_1 r_1)} \quad (13)$$

The perturbation flux can be obtained by the following integral

$$\phi_p(s)=\int_0^{r_1}\phi_{\varepsilon}^{p}(r,\ s)dr=\frac{1}{R_1}\left(F_1^{p}(s)-\frac{NI_bR_1^0}{R^0}\cdot\frac{g_p(s)}{g_n}\right) \quad (14a)$$

where R_1 is the effective reluctance of Element 1 with nominal air gap g_n

Using the same approach employed above, one can show that for Element 3

$$\phi_p(s)=\frac{1}{R_3}\left(F_3^{p}(s)-\frac{NI_bR_3^0}{R^0}\cdot\frac{g_p(s)}{g_n}\right) \quad (14b)$$

where R_3 is the effective reluctance of Element 3 with nominal air gap g_n, and $F_3^{p}(s)$ is the magnetomotive force across this element. From [1], we know that for Element *i*, *i*=2, 4, 5 and 6

$$\phi_p(s)=\frac{1}{R_i}F_i^{p}(s) \quad (14c)$$

where R_i is the effective reluctance of Element *i*, $F_i^{p}(s)$ is the magnetomotive force across Element *i*. Therefore, we have,

$$F_i^{p}(s)=R_i\phi_p(s)+\frac{NI_bR_i^0}{R^0}\cdot\frac{g_p(s)}{g_n}, \text{ when } i=1, \text{ and } 3 \quad (15a)$$

$$F_i^{p}(s)=R_i\phi_p(s), \text{ when } i=2, 4, 5 \text{ and } 6 \quad (15b)$$

The magnetomotive force across each element consists of a bias term and a perturbation term,

$$F_i(s)=F_i^{b}+F_i^{p}(s) \quad (16)$$

where the bias terms are constant. According to Ampere's law,

$$\sum_{i=1}^{6}F_i(s)=NI(s) \quad (17a)$$

while for the bias static field

$$\sum_{i=1}^{6}F_i^{b}=NI_b \quad (17b)$$

therefore

$$\sum_{i=1}^{6}F_i^{p}(s)=NI_p(s) \quad (18)$$

where $I_p(s)$ is the perturbation current, $I_p(s)=L\{i(t)-i_b\}$. Substituting (15) into (18) yields

$$\phi_p(s)\cdot\sum_{i=1}^{6}R_i+\frac{NI_bR_1^0}{R^0}\cdot\frac{g_p(s)}{g_n}+\frac{NI_bR_3^0}{R^0}\cdot\frac{g_p(s)}{g_n}=NI_p(s) \quad (19)$$

Noting $R_1^0=\frac{g_n}{\mu_0 A_1}$ and $R_3^0=\frac{g_n}{\mu_0 A_2}$, where A_1 and A_2 are the cross sectional areas of the inner and outer poles respectively, one can obtain

$$\phi_p(s)=\frac{N}{\sum_{i=1}^{6}R_i}I_p(s)-\frac{1}{\mu_0}\left(\frac{1}{A_1}+\frac{1}{A_2}\right)\frac{NI_b}{R^0}\frac{1}{\sum_{i=1}^{6}R_i}g_p(s) \quad (20a)$$

From the treatment in [1], the simplified model of (20a) is

$$\phi_p(s)=\frac{N}{R^0+c\sqrt{s}}I_p(s)-\frac{1}{\mu_0}\left(\frac{1}{A_1}+\frac{1}{A_2}\right)\frac{NI_b}{R^0}\frac{1}{R^0+c\sqrt{s}}g_p(s) \quad (20b)$$

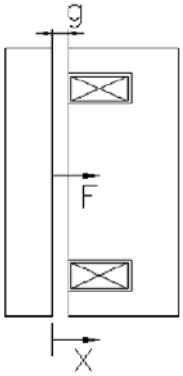

Fig. 5: Directions of the Mechanical Force and Displacement

According to the direction of mechanical force shown Fig. 5, $X_p=-g_p$

$$\phi_p(s)=\frac{N}{R^0+c\sqrt{s}}I_p(s)+\frac{1}{\mu_0}\left(\frac{1}{A_1}+\frac{1}{A_2}\right)\frac{NI_b}{R^0}\frac{1}{R^0+c\sqrt{s}}X_p(s) \quad (20c)$$

From [1], we know that the total mechanical force $f(t)$ is

$$f(t) = \frac{1}{2\mu_0}\oint_S B^2(t,r)ds \qquad (21)$$

where $B(t,r)$ includes bias and perturbation terms.

Therefore, the total mechanical force also consists of bias and perturbation terms

$$f(t) = f_b + f_p(t) \qquad (22)$$

Assuming perturbation flux density is small, we have

$$f_p(t) = \frac{1}{\mu_0}\left(\frac{1}{A_1}+\frac{1}{A_2}\right)\cdot\frac{NI_b}{R^0}\cdot\phi_p(t) \qquad (23)$$

Taking Laplace transform of (23) yields

$$F_p(s) = K_\phi \cdot \phi_p(s) \qquad (24)$$

where $K_\phi = \frac{1}{\mu_0}\left(\frac{1}{A_1}+\frac{1}{A_2}\right)\cdot\frac{NI_b}{R^0}$, and we notice that K_ϕ also appears in (20). Combining (20c) and (24) yields

$$F_p(s) = \frac{K_\phi N}{R^0 + c\sqrt{s}} I_p(s) + \frac{K_\phi^2}{R^0 + c\sqrt{s}} X_p(s) \qquad (25a)$$

Equation (25a) can written as

$$F_p(s) = K_i \cdot \frac{R^0}{R^0 + c\sqrt{s}} \cdot I_p(s) + K_x \cdot \frac{R^0}{R^0 + c\sqrt{s}} \cdot X_p(s) \qquad (25b)$$

where

$$K_i = \frac{K_\phi N}{R^0}, \text{ and } K_x = \frac{K_\phi^2}{R^0} \qquad (25c)$$

for the solid actuator. Equation (25b) shows that in a solid magnetic actuator, due to the appearance of eddy currents, both current stiffness and displacement stiffness are attenuated at the rate of a half-order of frequency. From (25b), one can develop a block diagram representation for a solid magnetic actuator operated in current mode, as shown in Fig. 6

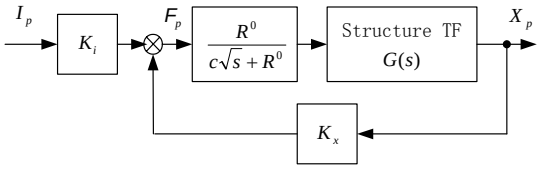

Fig. 6: Block Diagram for a Solid Actuator Operated in the Current Mode

III. EXPERIMENT

In order to examine the accuracy of the analytic model developed in section 2 and to investigate the performance of robust controllers that will be designed in a future research effort, a test rig, shown in Fig. 7, was carefully designed, built and calibrated.

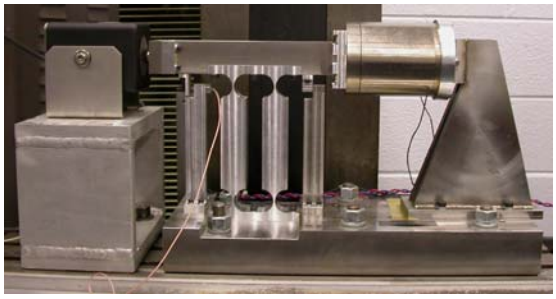

Fig. 7: The Test Rig

The primary objective in experiment design was to develop a system that could be easily modelled from a mechanical viewpoint, yet still encompasses all the important characteristics of magnetic levitation systems using solid actuators.

In the test rig, a beam, supported by a compliant aluminium flexure, is allowed one degree of freedom translation. A solid magnetic actuator and a shaker, located on each end of the beam, provide control forces. The flotor and the stator of the magnetic actuator are attached to the beam and the actuator stand respectively by adapters. The actuator stand is bolted down to a steel base plate. The shaker is attached to the beam by two C shaped adapters, and is bolted down to the shaker base. Both the base plate and shaker base are attached to a surplus milling machine bed for a foundation.

The rigorous model (25b) for cylindrical actuators shows that the eddy current effects on actuator dynamics may be represented by the coefficient, *c*, of the half-order term. It is desirable to examine how the analytic model fares in comparison to experimental results. Towards this end, a swept sine test was conducted to determine experimentally the frequency response of the transfer function, X_p / I_p, see Fig. 8

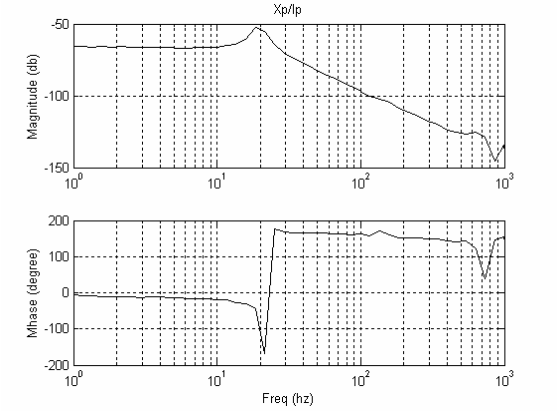

Fig. 8: A Swept Sine Test Result of X_p / I_p

According to the block diagram of the experimental test rig shown in Fig. 9,

$$\frac{X_p}{I_p} = \frac{R^0 K_i}{cms^{5/2} + R^0 ms^2 + cc_d s^{3/2} + R^0 c_d s + cKs^{1/2} + R^0(K - K_x)} \quad (26)$$

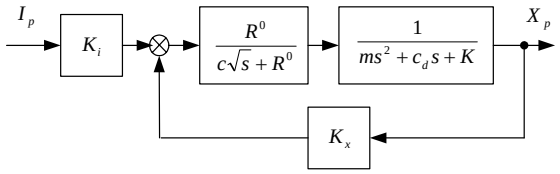

Fig. 9: Block Diagram of the Experimental Test Rig

We conducted calibration tests to determine all the parameters within this model with the exception of the eddy current effect coefficient *c*. Then, an estimate of *c* can be obtained using the frequency domain identification approach presented in [3]. Table 1 lists the calibration values of all the parameters in (26) with the exception of eddy current coefficient *c*.

Table 1 Parameter in (26) Except *c*

m	$2.205kg$
c_d	$20.014Ns/m$ (from Swept Sine Test of the Structure)
K	$34924N/m$
K_x	$5478N/m$
K_i	$18.67N/A$
g	$20.1mil$
μ_r	9000 (from Rowland Ring Test)

Employing the frequency domain identification approach in [3] on (26) with the calibrated parameters in Table 1 and the experimental frequency response data from 1 to 300hz, the identified value of the eddy current coefficient is $c_I = 12878\, ampere/webber$ (Superscript I indicates the identified value). From [1], we have a theoretical value $c_T = 14710\, ampere/webber$. Fig. 10 shows the frequency response of the transfer function $\frac{R^0}{c\sqrt{s}+R^0}$ with $c = c_I$ and with $c = c_T$. Fig. 11 and 12 presents a comparison among the experimental data of $X_p(s)/I_p(s)$, theoretical values calculated from (26) with $c = c_I$, with $c = c_T$, and with $c = 0$. Figure 10-12 show that the eddy current effect predicted by the analytic model from (25b) is very close to what was observed from experimental tests, thus indicating the accuracy of the analytic model.

For further model comparison, a swept sine test was conducted to obtain the frequency response of $A(s)/I_p(s)$, where $A(s)$ is acceleration of the beam. Theoretical values calculated with $c = c_I$, with $c = c_T$ and with $c = 0$ for $A(s)/I_p(s)$ were compared with the experimental data in Fig. 13 and 14. This again demonstrates the accuracy of the analytic model.

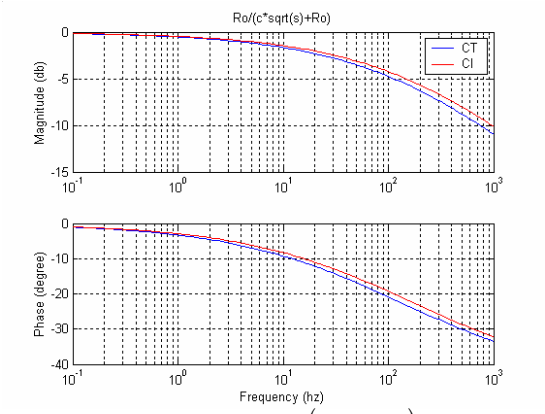

Fig. 10: Frequency Response of $R^0/\left(c\sqrt{s}+R^0\right)$ with $c = c_I$ and with $c = c_T$

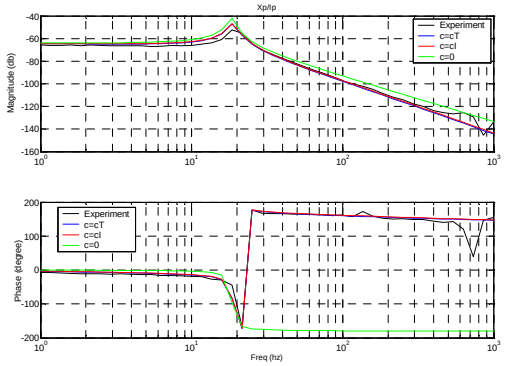

Fig. 11: Experimental Data and Theoretical Values for X_p / I_p

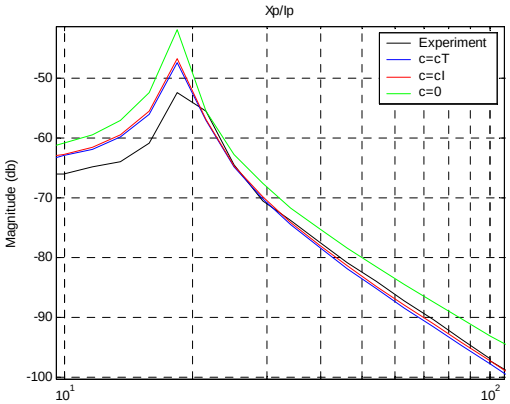

Fig. 12: Zoom-in View on the Magnitude plot in Fig. 11

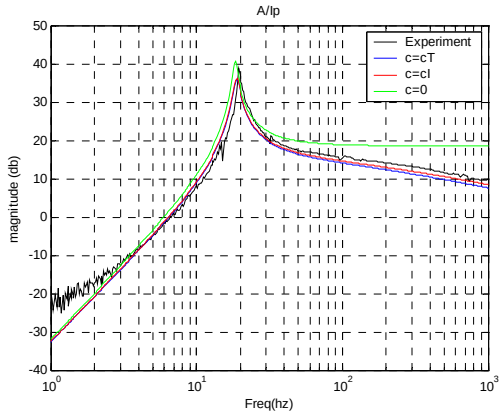

Fig. 13: Experimental Data and Theoretical Values for A/I_p - Magnitude Plot

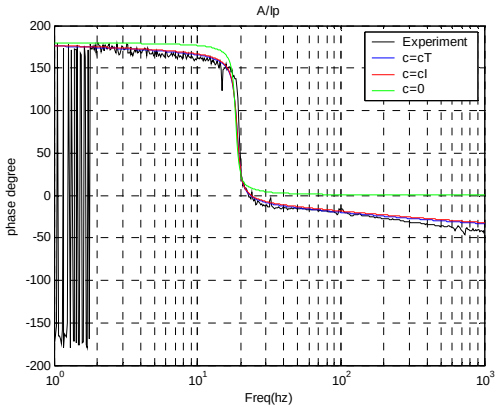

Fig. 14: Experimental Data and Theoretical Values for A/I_p -Phase Plot

IV. Conclusion

In this paper, the effect of changing air gap length on mechanical force produced by a solid cylindrical magnetic actuator was studied by adopting the magnetic field analysis approach developed in [1]. A complete analytic model, which shows the effect of eddy currents on both the displacement stiffness and the current stiffness, was derived. Experiments conducted prove the accuracy of the model.

References

[1] L. Zhu, C. Knospe, and E. Maslen "An analytic model for a non-laminated cylindrical magnetic actuator with eddy currents" *IEEE Trans. Magnetics.* vol. 41, No. 4, pp. 1248- 1258, April. 2005.

[2] L. Zhu, C. R. Knospe, and E. H. Maslen, "Frequency domain modeling of non-laminated c-shaped magnetic actuators", The Ninth International Symposium on Magnetic Bearings, 2004.

[3] E.C. Levi, "complex-curve fitting," *IRE Trans. on Automatic Control*, Vol. AC-4 (1959), pp. 37-44